Time-Iterative Solutions of Viscous Supersonic Nozzle Flows

Chau-Lyan Chang,* Yigal Kronzon,† and Charles L. Merkle‡
Pennsylvania State University, University Park, Pennsylvania

Supersonic viscous flows in high-expansion ratio rocket nozzles are studied numerically using the thin-layer Navier-Stokes equations. A discretization scheme using upwind flux-vector split differencing in the streamwise direction and central differencing in the cross-stream direction is chosen. Of the three implicit approximate factorization schemes considered, the diagonally dominant alternating direction and the parabolized alternating direction methods are found to be much faster than standard alternating direction procedures. The optimum Courant numbers for these methods are about 500 and produce convergence rates that rival direct methods. Proper downstream boundary conditions for the subsonic portion of the outflow are shown to allow control over the exit boundary-layer thickness, including recirculating flows with re-entry conditions at the exit plane. Representative nozzle flowfields are shown for conical and contoured nozzles for different Reynolds numbers, wall temperatures, and back pressure and for both laminar and turbulent flows. Excellent global mass conservation is demonstrated when the strongly conservative equations are used, but the quasiconservative equations lead to conservation errors that are unacceptably large. The computed results for a typical high Reynolds number flow through the high-expansion nozzle are compared to the Method of Characteristics (MOC) prediction with good agreement.

Introduction

THE focus of the present research is directed toward developing accurate numerical algorithms for predicting the viscous supersonic flowfields that occur in advanced rocket exhaust nozzles. The geometrical configurations of interest include both the smoothly diverging sections that are traditionally associated with nozzles as well as other more nontraditional shapes that contain discontinuities that give rise to regions of separated flow. The thrust levels of interest range from very low to very high values so that the Reynolds number range is equally broad. For these reasons, our focus is on the Navier-Stokes equations rather than the parabolized Navier-Stokes (PNS) equations that are more commonly applied to similar supersonic viscous flows.[1-4] The variety of flowfields does include, however, flows that are aptly described by the PNS equations, and the emphasis is on developing a Navier-Stokes solver that becomes more efficient as the size of the subsonic region diminishes and upstream effects become less significant.

Several specific aspects of the solution of the Navier-Stokes equations are considered. We begin with an assessment of those algorithms that take into account the predominantly hyperbolic nature of the flowfield and consequently promise to provide rapid convergence in the high Reynolds number, unseparated flow limit. Because of our interest in lower Reynolds numbers, we also consider the implementation of proper downstream boundary conditions on the subsonic portion of the exit profile and the impact these boundary conditions have on the solution. Finally, because one of the ultimate goals of nozzle flowfield prediction is to predict thrust accurately, we also pay strict attention to the degree to which global mass conservation is enforced. The results of numerical experiments show that this mass conservation requirement dictates the use of the strong conservation form of the equations and, in particular, that the "quasiconservative" forms of the equations introduce global conservation errors of order unity even for continuous solutions and, hence, are not acceptable. Although our long-term interests are for three-dimensional flows, all of the present results are for axisymmetric geometries.

The examples chosen to demonstrate the techniques are limited to two nozzle shapes, a conical nozzle and a high area ratio contoured nozzle. Other variations of flowfield character are obtained by varying the pressure level (nozzle Reynolds number), wall temperature, and nozzle back pressure. In particular, back pressures that are sufficiently high to produce separation inside the nozzle are considered in order to simulate the classical experimental characteristics observed when altitude nozzles are operated on sea-level thrust stands. The examples include both laminar and turbulent flow calculations. The turbulent calculations are based upon the Baldwin-Lomax turbulence model.[5-7]

Algorithms for Viscous Supersonic Flow

Discretization of the Equations

The hyperbolic nature of supersonic flows allows inviscid problems to be computed in a single pass. This capability is lost in viscous flows for two reasons. The first is streamwise diffusion, but this is weak for high and even moderate Reynolds number flows and may frequently be neglected. The second and more significant reason is the subsonic region adjacent to the walls, and it is on this aspect of upstream influence that our attention is concentrated. From a physical viewpoint, this subsonic region allows acoustic waves to propagate upstream. From a numerical aspect, it renders space-marching schemes unconditionally unstable. In the parabolized Navier-Stokes approximation, these upstream effects are removed so that single-pass solutions are allowed. Our interests are with those problems for which this upstream effect must be retained, even though part or all of the subsonic layer may be thin. This aspect of the problem is generally referred to as the global PNS iteration.[8-10] Here, we attempt the global iteration from the Navier-Stokes equations and, consequently, pose the problem as a time-marching problem.

Received May 5, 1987; presented as Paper 87-1289 at the AIAA 19th Fluid Dynamics, Plasma Dynamics, and Lasers Conference, Honolulu, HI, June 8–10, 1987; revision received Feb. 22, 1988.

*Graduate Assistant, Department of Mechanical Engineering.
†Research Associate, Department of Mechanical Engineering.
‡Distinguished Alumni Professor, Department of Mechanical Engineering.

In discretizing the equations, we take advantage of the predominantly supersonic character of the flowfield by using flux-vector splitting[11] in the streamwise direction while retaining central differencing in the cross-stream directions. Using Euler implicit differencing in time, the result can be expressed symbolically as

$$\frac{\partial Q}{\partial t}+\left(\frac{\partial E^{+}}{\partial \xi}+\frac{\partial E^{-}}{\partial \xi}+\frac{\partial F}{\partial \eta}-H\right)^{n+1}=0 \tag{1}$$

where the superscript $n+1$ implies that these quantities are to be evaluated at the new time level. Here, E^{+} and E^{-} represent the (split) streamwise flux vector, while F is the flux vector in the cross-stream direction and H is the source term that arises because of the axisymmetric geometry. With the equations written in generalized coordinates as suggested in Eq. (1), these vectors take on the form

$$E^{+}+E^{-}=\frac{y}{J}\begin{bmatrix}\rho U\\ \rho u U+\xi_x p\\ \rho v U+\xi_y p\\ (e+p)U\end{bmatrix} \tag{2a}$$

$$H=\frac{1}{J}\begin{bmatrix}0\\ \dfrac{-2}{3}\eta_x\dfrac{\partial}{\partial\eta}\mu v\\ p-\dfrac{4}{3}\mu\dfrac{v}{y}+\dfrac{2}{3}\mu\eta_x\dfrac{\partial u}{\partial\eta}-\dfrac{2}{3}v n_y\dfrac{\partial\mu}{\partial\eta}\\ \dfrac{-2}{3}\eta_x\dfrac{\partial}{\partial\eta}\mu u v-\dfrac{2}{3}\eta_y\dfrac{\partial}{\partial\eta}\mu v^2\end{bmatrix} \tag{2b}$$

and $F=F_I+F_v$ where

$$F_I=\frac{y}{J}\begin{bmatrix}\rho V\\ \rho u V+\eta_x p\\ \rho v V+\eta_y p\\ (e+p)V\end{bmatrix} \tag{2c}$$

$$F_v=\frac{y}{J}\begin{bmatrix}0\\ \alpha_1\dfrac{\partial u}{\partial\eta}+\alpha_2\dfrac{\partial v}{\partial\eta}\\ \alpha_2\dfrac{\partial u}{\partial\eta}+\alpha_3\dfrac{\partial v}{\partial\eta}\\ \alpha_4\dfrac{\partial}{\partial\eta}\dfrac{e}{\rho}+\dfrac{\alpha_1-\alpha_4}{2}\dfrac{\partial u^2}{\partial\eta}+\dfrac{\alpha_3-\alpha_4}{2}\dfrac{\partial v^2}{\partial\eta}+\alpha_2\dfrac{\partial uv}{\partial\eta}\end{bmatrix} \tag{2d}$$

with

$$\alpha_1=\mu(4/3\,\eta_x^2+\eta_y^2),\qquad \alpha_2=\mu/3\,\eta_x\eta_y \tag{2e}$$

$$\alpha_3=\mu(\eta_x^2+4/3\,\eta_y^2),\qquad \alpha_4=\gamma k(\eta_x^2+\eta_y^2)/Cp \tag{2f}$$

The primary dependent variable Q is given as

$$Q=y/J\,(\rho,\rho u,\rho v,e)^T \tag{3}$$

where J is the Jacobian of the transformation. In these equations, x and y represent the axial and radial coordinates in the untransformed axisymmetric coordinate system, while ξ and η are their counterparts in the transformed system. Standard notation is used for the flowfield variables.

On splitting the streamwise flux vector E, the quantities E^{+} and E^{-} in Eq. (1) are upwind-differenced according to the sign of their individual eigenvalues. This upwind-centered differencing combined with the streamwise flux vector splitting provides an algorithm that is identical to typical PNS schemes in the supersonic part of the stream where E^{-} vanishes. In such supersonic regions, the algorithm provides a matrix structure that allows marching in ξ. The difficulty is that the supersonic region is coupled to the subsonic region where upstream influences exist. Consequently, both regions must be computed multiple times. We have considered several methods for solving Eq. (1) at each time step, as will be outlined next.

Solution of the Equations by Standard Alternating Direction Implicit (ADI) Procedures

The use of upwind differencing traditionally provides a much richer choice of solution methods than does central differencing, and the present problem is no exception. A number of procedures can be identified for solving the operator in Eq. (1). Of these, we discuss three approximate factorization methods and one exact procedure. The first of the approximate procedures is standard approximate factorization.[12,13] In this procedure, the ξ and η directions are split, and the discretized version of Eq. (1) in delta form becomes

$$\left[I-D\Delta t+\Delta t\left(\frac{\partial}{\partial\xi}A^{-}+\frac{\partial}{\partial\xi}A^{+}\right)\right](I-D\Delta t)^{-1}\times\left[I-D\Delta t+\Delta t\frac{\partial B}{\partial\eta}\right]\Delta Q=-\Delta t R \tag{4}$$

were $D=\partial H/\partial Q$, A^{+} and A^{-} represent the split parts of the Jacobian $A=\partial E/\partial Q$, and B is used symbolically to represent the sum of inviscid and viscous terms in η. The vector R is the residual evaluated at time level n:

$$R=\left(\frac{\partial E^{+}}{\partial\xi}+\frac{\partial E^{-}}{\partial\xi}+\frac{\partial F}{\partial\eta}-H\right)^{n} \tag{5}$$

The solution of Eq. (1) by the algorithm given in Eq. (4) is standard and requires no further comment.

Diagonally Dominant ADI Procedure

A second approximate factorization procedure is the diagonally dominant alternating direction implicit (DDADI) procedure developed by Lombard et. al.[14,15] This method has also been referred to as a linear Gauss-Seidel relaxation by Chakravarthy[16] and MacCormack.[17] To express this algorithm, we must discretize the equation in ξ as well as t. Explicit discretization in η is not needed to specify the algorithm, and again central differencing in η is only implied. Although our calculations are for second-order upwind differencing in ξ, for simplicity we use first-order upwind differencing to demonstrate the algorithm. The philosophy of the DDADI procedure is to place as many terms as possible on the diagonal before factoring. Upon discretizing in ξ and approximately factoring, we obtain

$$\left[I-\Delta tD-\frac{\Delta t}{\Delta\xi}A_{ij}^{-}+\Delta t\frac{\partial}{\partial\xi}A^{+}+\Delta t\frac{\partial}{\partial\eta}B\right]\times\left[I-\Delta tD+\frac{\Delta t}{\Delta\xi}(A_{ij}^{+}-A_{ij}^{-})\right]^{-1}\times\left[I-\Delta tD+\frac{\Delta t}{\Delta\xi}A_{ij}^{+}+\Delta t\frac{\partial}{\partial\xi}A^{-}+\Delta t\frac{\partial}{\partial\eta}B\right]\Delta Q=-\Delta t R \tag{6}$$

For consistency with the notation in Eq. (4) we have retained nondiscretized terms where possible, but this algorithm cannot be written in its entirety without performing some discretization in space. Accordingly, the terms like $\partial/\partial\xi\,A$ [both here and in Eq. (4)] are to be discretized by upwind differencing in the proper direction. The terms with subscripts and a finite increment in ξ (e.g., $A_{ij}/\Delta\xi$) are terms that have already

been discretized. Here, the subscripts imply that the matrix A is to be evaluated at the (diagonal) grid point.

The backward differencing used to evaluate $\partial A^+/\partial\xi$ implies that the first operator can be solved by marching from the nozzle throat to the exit plane. Each ξ plane requires the solution of a block-tridiagonal matrix. Similarly, the last operator can be solved by marching forward from the nozzle exit. Several minor variations of this formulation have also been used.

PNS-ADI Procedure

The third approximate factorization procedure considered is also a forward-backward scheme designed to give a PNS-like sweep in the forward direction and a partial backward sweep that is required only in those regions where the flow is subsonic. Because of its analogy with PNS algorithms, this procedure is referred to as a PNS-ADI scheme. The scheme can again be described by discretizing in time only and can be expressed as

$$\left(I - D\Delta t + \Delta t\frac{\partial}{\partial\xi}A^+ + \Delta t\frac{\partial}{\partial\eta}B\right)(I - \Delta tD)^{-1} \times\left(I - \Delta tD + \frac{\partial}{\partial\xi}A^-\right)\Delta Q = -\Delta t\boldsymbol{R} \tag{7}$$

As indicated, the first operator is exactly the (time-dependent version of) a typical PNS procedure, whereas the last operator reduces to the identity operator in supersonic regions where A^- vanishes but is bidiagonal in subsonic regions. Thus, in supersonic flows the PNS-ADI procedure becomes a marching procedure, but in subsonic regions it retains the influence of the upstream acoustic wave.

Direct Solution by Flowfield Partitioning

The predominantly supersonic character of high Reynolds number nozzle flows gives rise to a flowfield that can be solved almost entirely by space marching. Only the thin subsonic portion of the boundary layer prevents this very efficient computational technique. Recognition of the physical character of such flows suggest the partitioning shown in Fig. 1 that separates the subsonic and supersonic regimes. The flowfield is partitioned into three parts, domains A, B, and C. Domain A is composed only of points that are supersonic. Domain B includes all subsonic points in the field as well as some that are supersonic. Domain C is the single row of grid points that divides domains A and B. In principle, domain B could be chosen to include only the subsonic points, but then domain C would be an irregular line through the field, and the present regular partitioning is chosen for simplicity.

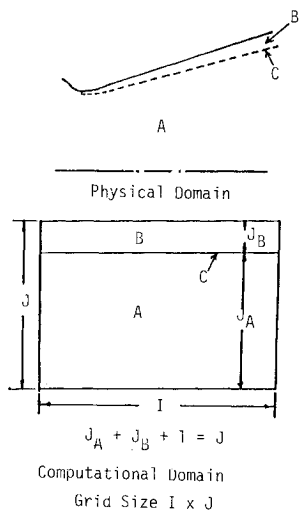

Fig. 1 Partitioning of physical and computational domain: domain A is entirely supersonic; domain C is a line of all supersonic points; domain B includes all subsonic points in the flowfield.

This partitioning allows a direct solution procedure that does not depend upon approximate factorization. The advantage of direct solution methods is that they allow the full advantages of an implicit algorithm to be realized. In a direct implicit method, the optimum Courant-Friedrichs-Lewy (CFL) condition is unbounded on an infinite precision machine, while for finite precision calculations it lies in the range of 10^6–10^{10}. For most approximately factored algorithms, the optimum CFL for either infinite or finite precision arithmetic lies in the range of 10–100. These small values of CFL result in much slower rates of convergence than can be expected for direct procedures. Some preliminary results of this technique are shown in the following section, but the details of the algorithm are given elsewhere.[18]

Algorithm Comparisons

The four methods described are concerned with using different algorithms to solve the same equations. The residual on the right-hand side of Eqs. (4), (6), and (7) is identical, both in terms of the partial differential equation representation and the finite-difference representation. When the vari-

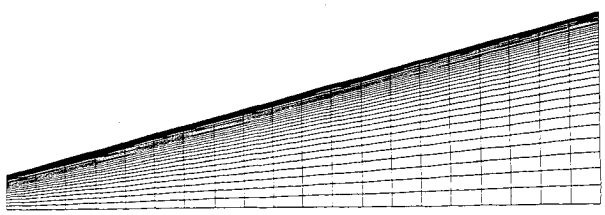

Fig. 2 15-deg conical nozzle for convergence comparison: grid size 21 × 40; area ratio 30.

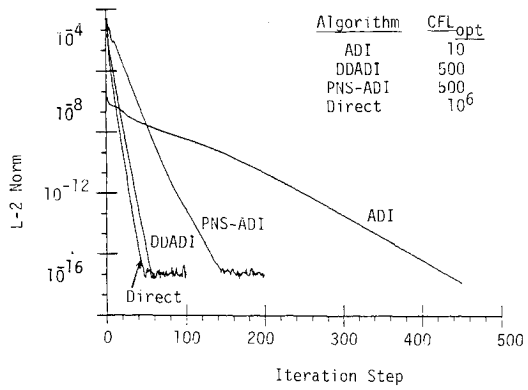

Fig. 3 Convergence based on number of iterations (starting from PNS).

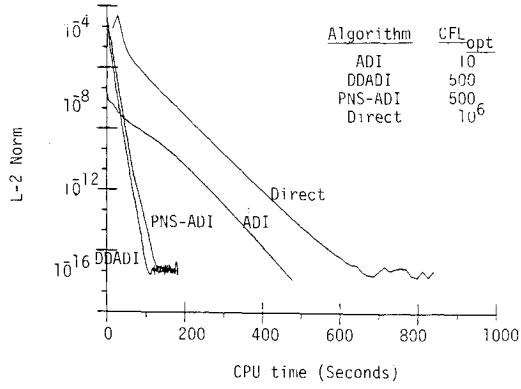

Fig. 4 Convergence based on CPU time (starting from PNS).

able ΔQ is driven to zero, all four methods provide identical solutions. (A check of their converged solutions shows that they are identical to six or seven digits.) Because the algorithms differ only in the path that they take to arrive at the solution, the only relevant comparisons are ones that compare their rates of convergence. In this regard, it is of interest to compare both the number of iterations required to reach convergence and the amount of CPU time required. The number of iterations required tells something of their convergence efficiency, while the CPU requirements convey something of their relative cost per step. This latter result will be affected both by the number of arithmetic operations per step and by the type of computer architecture used for the calculations. Our present results are for a scalar machine. Slightly different conclusions may be reached for calculations on vector machines.

As a test problem for comparison of the algorithms, the laminar supersonic flow through a 15-deg conical nozzle with an expansion ratio of 30 was used. The nozzle geometry and the 21 (axial) by 40 (cross-stream) grid are shown in Fig. 2. As a starting line, a constant Mach number flow ($M = 1.02$) with zero contravariant velocity was chosen. Although this is not as realistic as a two-dimensional initial line, it provides a well-defined problem. Our experience, however, has shown that accurate representation of the wall heat flux (which is seldom well known) is much more significant in high-expansion ratio nozzles than is the two-dimensionality on the inlet line. The nozzle Reynolds number based on the throat radius was 10^5. The converged solution showed that with this highly stretched grid the subsonic portion of the boundary layer had grown to nine points at the exit plane. The calculations were done without artificial viscosity, except for that inherent in the upwind differencing in x.

Convergence rates for the four algorithms are shown in Figs. 3 and 4. Figure 3 shows the rate of convergence of each of the methods in terms of the number of iterations required. Figure 4 presents the CPU requirements on a scalar processor (IBM 3090) in double precision. The linear convergence on the semilogarithmic plot until machine accuracy is reached gives additional verification that the codes are error free. All calculations were started from initial conditions, which were obtained by using a single forward sweep through the flowfield with the PNS-ADI algorithm [Eq. (7)]. Results shown for each scheme correspond to the optimum CFL for this scheme. These optimums are shown in the figure. Note that the DDADI method is almost as fast in number of iterations as the direct procedure and is competitive with the PNS-ADI method in terms of CPU time. These latter two methods would also be expected to be most efficient on a vector processor.

In terms of number of iterations required, the ADI scheme is seen to be the slowest by far. It also has the lowest optimum value of CFL (10). The DDADI scheme is the fastest of the three approximate methods and converges almost as rapidly as the direct method. Both the DDADI and the PNS-ADI algorithms converged most rapidly at CFL = 500. A comparison of the number of terms contained in the approximate factorization errors for these three schemes correlates directly with these convergence results.

The convergence rate for the direct procedure was somewhat disappointing in that it required 40 iterations to reach machine accuracy. The optimum CFL for the direct case was about 10^6, although the convergence was independent of CFL up to at least 10^{10}. Our previous experience with direct procedures has shown a consistent convergence to machine accuracy in 8–11 iterations at these CFL's, but this "normal" convergence rate could not be attained here.

The corresponding CPU times for convergence are shown in Fig. 4. The direct method is seen to require the most time, but if we could attain the factor of four improvement noted earlier, it would be competitive with the faster procedures. In terms of CPU time, the PNS-ADI and DDADI schemes are quite competitive and are about a factor of three faster than standard ADI. Tests of convergence rates with number of grid points showed that the three approximate methods required a small increase in number of iterations (about 10%) each time the grid density was doubled in each direction. For example, the contoured nozzle shown later with a 75 × 50 grid required 80 steps to reach machine accuracy with the DDADI method.

Nozzle Flowfield Predictions

To demonstrate the capabilities of the upwind-central difference combination, the flowfields in two nozzle geometries were computed. The first geometry was the 15-deg conical nozzle shown in Fig. 2, except that here a 21 × 70 grid was used. The second nozzle was the contoured geometry shown in Fig. 5, with a grid of 75 × 50. The area ratio of this nozzle was 272 : 1.

Flowfield calculations for both nozzles were run at stagnation pressures of 3.5 and 35 atm. In both nozzles, a throat radius of 10 mm was chosen so that these pressures corresponded to nozzle throat Reynolds numbers of 1.4×10^4 and 1.4×10^5, respectively. All calculations in the conical nozzle were for laminar flow; those in the contoured nozzle were for both laminar and turbulent flow. Properties of rocket combustion gases ($\gamma = 1.24$, $C_p = 3043$ J/kg K) were used for all calculations. A stagnation temperature of 3500 K was used throughout. The calculations presented below were obtained with either the DDADI or the PNS-ADI algorithms.

Effects of Downstream Boundary Conditions

The schemes described above all require a downstream boundary condition for the subsonic part of the boundary layer. Previous researchers have generally ignored this boundary condition and computed the appropriate parameters by extrapolation from inside the computational domain. Although this provides solutions when the subsonic layer is thin, it will fail if the subsonic layer becomes thick. Furthermore, an extrapolated boundary condition does not allow flowfields to respond to downstream conditions as they must in physical situations. In the case of nozzle flows, a high back pressure can cause the boundary layer to thicken and the flow to separate. A case in point is a high-expansion ratio nozzle operated at sea level static conditions on a test stand. Calculation of this effect requires that the pressure boundary condition be imposed on the subsonic part of the exit boundary. Perhaps it is more important to be able to simulate the effect of back pressure on the nozzle lip region because this phenomenon can represent a notable correction from altitude test stands to operation in space.

Results of a series of calculations in which the pressure at the subsonic part of the outflow boundary was specified are shown in Figs. 6–9. The pressure boundary condition is imposed by a Method of Characteristics (MOC) procedure. The exit line is split into inflow and outflow sections depending on the solution at the previous time step. Outflow grid points are treated as hyperbolic, and all information is obtained from inside the domain using one-sided, second-order-accurate differencing. For grid points with inflow, the ambient static pressure and temperature are taken as stagnation conditions for an inflow boundary. These inflow boundary conditions are specified by a Method of Characteristics procedure identical to that used for inflow boundaries in Ref. 19. In

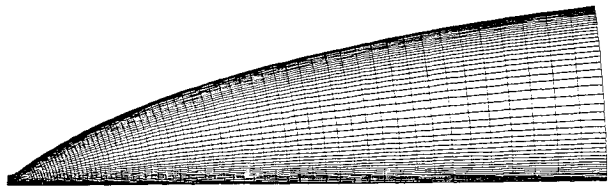

Fig. 5 Contoured nozzle geometry: 75 × 50 grid; area ratio 272 : 1.

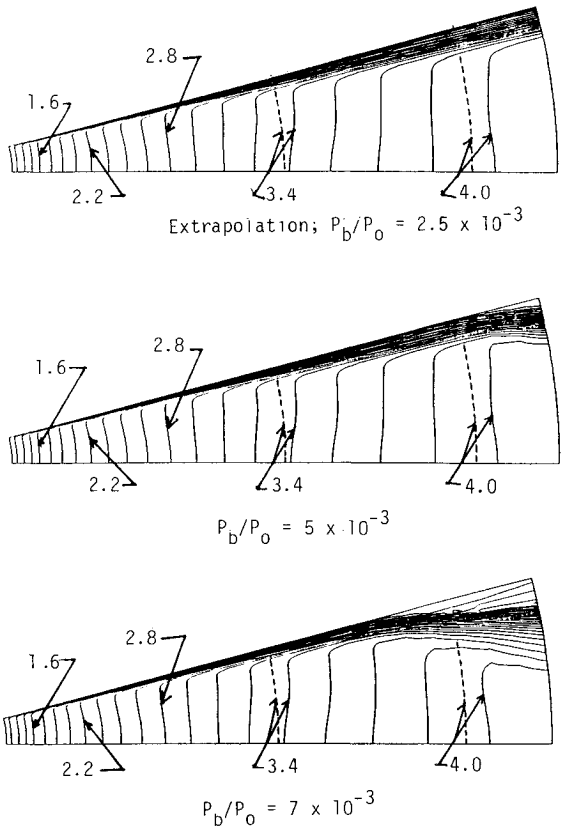

Fig. 6 Converged Mach number contours for conical nozzle using various back pressures: one-dimensional exit pressure, $p_e/p_o = 2.7 \times 10^{-3}$; dashed line indicates one-dimensional inviscid results.

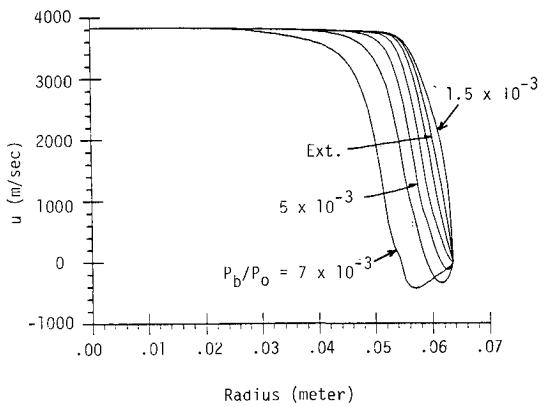

Fig. 7 Velocity profile at nozzle exit plane for conical nozzle and various back pressure; $p_o = 3.5$ atm.

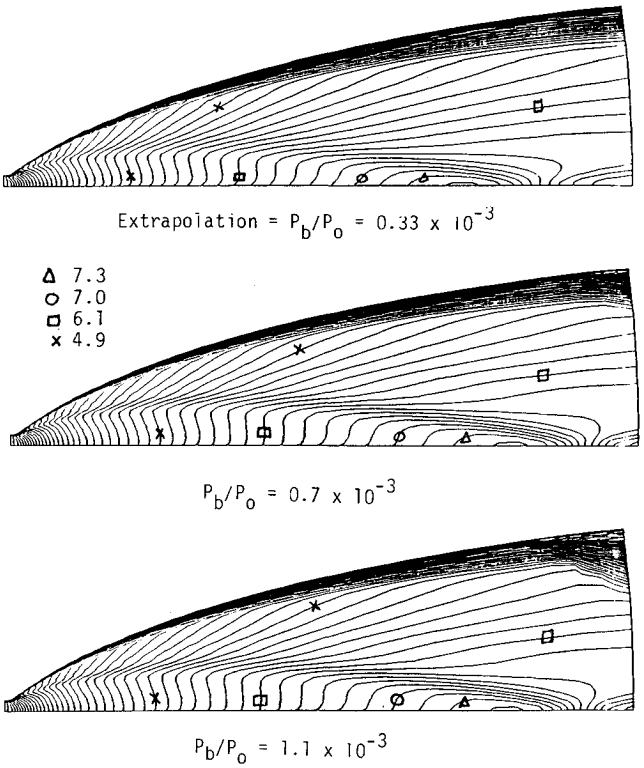

Fig. 8 Turbulent flow calculation in 272 : 1 contoured nozzle: 75 × 50 grid: $p_o = 35$ atm; $Re = 1.4 \times 10^5$.

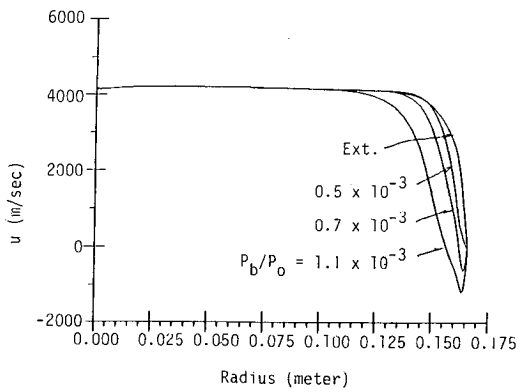

Fig. 9 Velocity profiles at exit plane for turbulent flow 272 : 1 contoured nozzle.

addition to specifying stagnation pressure and temperature, we also fix the flow angle. The fourth condition is obtained by using the downstream running characteristic information from inside the flowfield. Figure 6 shows Mach number contours for the conical nozzle at the lower Reynolds number. The top plot shows the results of using an extrapolation boundary condition. This boundary condition results in a back pressure to stagnation pressure ratio p_b/p_o of about 2.5×10^{-3}. The high Mach number gradient near the nozzle wall gives a visual indication of the boundary-layer thickness. The middle plot shows the effect of raising the back pressure to $p_b/p_o = 5 + 10^{-3}$. At this back pressure, the boundary layer at the exit has been thickened considerably, and a small recirculation zone is present. As the back pressure is increased, this recirculation region continues to grow and to propagate farther upstream, as indicated by the bottom plot, where $p_b/p_o = 7 \times 10^{-3}$. Corresponding calculations (not shown) show that reducing the back pressure below 2.5×10^{-3} causes the boundary layer at the exit plane to accelerate and become thinner. In all cases, the nominal length of upstream penetration of this effect was some one to two boundary-layer thicknesses, as might be expected. The wall temperature for these calculations was set at 3000 K.

As a comparison, the expansion obtained by one-dimensional, inviscid flow through this nozzle is also superimposed in Fig. 6. The effects of both viscosity and the recirculation region are to decrease the amount of expansion in the nozzle.

As a further indication of the character of these flows, the velocity profile at the exit plane for various back pressure levels is shown in Fig. 7. This plot clearly shows the manner in which the boundary layer thickens as p_b/p_o is increased and its rate of thinning as p_b/p_o is decreased. In addition, the magnitude and thickness of the re-entry region is shown. The re-entry flow is modeled by inlet boundary conditions, with a

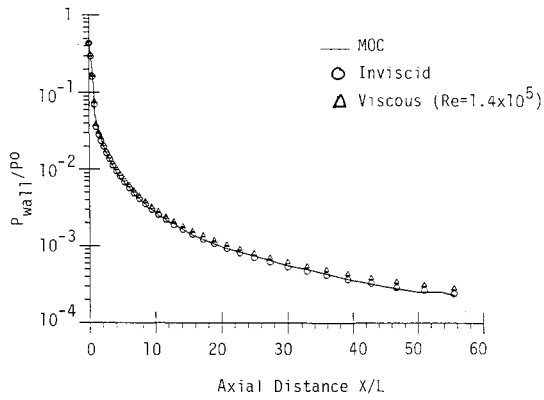

Fig. 10 Comparison of wall pressure distribution from present calculations with those from method of characteristics procedure.

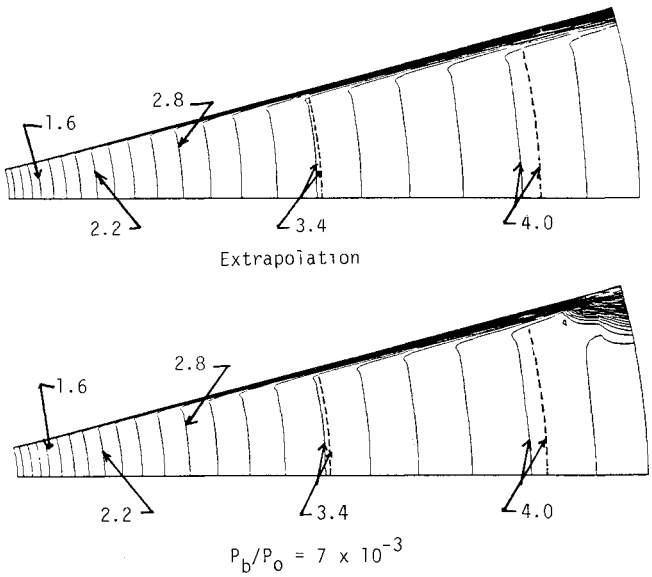

Fig. 11 Converged Mach number contours for conical nozzle at lower Reynolds number (1.4×10^4) and at cold-wall temperature $T_w = 300$ K for two back pressures: one-dimensional exit pressure, $p_e/p_o = 2.7 \times 10^{-3}$; dashed line indicates one-dimensional results.

stagnation pressure equal to the back pressure and a stagnation temperature equal to the wall temperature. To complete the inflow specification, the contravariant velocity V was set to zero.

Figure 8 shows results for turbulent flow in the contoured nozzle at the higher Reynolds number ($p_o = 35$ atm). Again, the topmost plot shows results for extrapolated boundary conditions, while the lower two plots are for higher back pressure. Extrapolation here corresponds to a back pressure of about $p_b/p_o = 3.3 \times 10^{-4}$. The middle plot is for a back pressure 7×10^{-4}, while the lower one is for 1.1×10^{-3}. Again, thickening and separation of the boundary layer is clearly seen, but here the turbulent character of the boundary layer requires a larger increase in p_b/p_o to obtain the same degree of separation. This point was verified by computing the same flowfield with laminar flow. When laminar boundary layers were used, the extrapolation boundary condition corresponded to a lower back pressure than in the turbulent case, because the much thinner laminar boundary layer allows more expansion to be accomplished in the nozzle. Also, the laminar boundary layer exhibited a larger separation region at $p_b/p_o = 7 \times 10^{-4}$ than did the turbulent boundary layer at 1.1×10^{-3}.

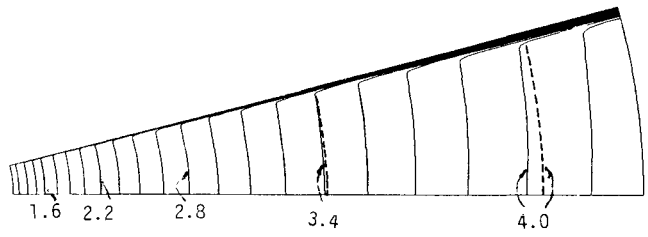

Fig. 12 Converged Mach number contours for high Reynolds number case ($p_o = 35$ atm), $T_w = 3000$ K: extrapolated downstream boundary conditions; dashed line shows one-dimensional results.

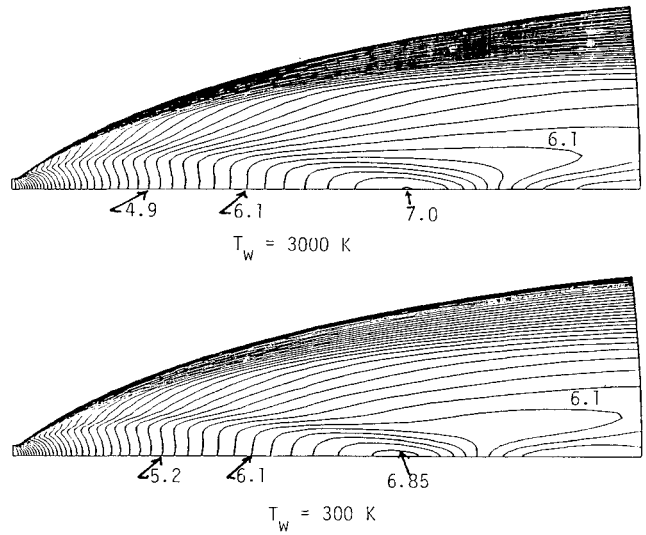

Fig. 13 Converged Mach number contours for 272 : 1 nozzle: $Re = 1.4 \times 10^4$; $p_o = 3.5$ atm.

The u velocity profiles at the exit plane for the turbulent case are shown in Fig. 9. Comparison with Fig. 7 shows these turbulent boundary layers to have fuller profiles with steeper gradients at the wall than their laminar counterparts. Note that the Mach number gradient in the inviscid portion of the exit plane in Fig. 8 is also present in this figure. The small scale and the relative insensitivity to velocity make the velocity profile appear nearly constant. To demonstrate the accuracy of the numerical solutions, we compare the wall pressure distributions obtained with the present procedure with results obtained from a MOC procedure.[20] Two comparisons are given in Fig. 10. First, the numerical results (circles) obtained with the present numerical procedure are compared with the MOC results. As can be seen, the two independent calculations give almost precisely the same results. The pressure distribution for the viscous case (triangles) at a Reynolds number of 1.4×10^5 (corresponding to $p_b/p_o = 0.33 \times 10^{-3}$ case in Fig. 8) are also shown. As can be seen, the presence of the boundary layer limits the expansion that is realized in the nozzle.

Effect of Reynolds Number and Wall Temperature

Although the previous discussion showed results for two different nozzle Reynolds numbers, some additional back-to-back comparisons of changes in Reynolds number are shown here along with comparisons of the effect of wall temperature. Figure 11 shows Mach number contours for the conical nozzle at the same Reynolds number as the results in Fig. 6. The top plot in Fig. 11 is for extrapolation conditions and corresponds to the top plot in Fig. 6. The bottom plot in Fig. 11 is for a back pressure of 7×10^{-3} and is analogous to the bottom plot in Fig. 6. The comparison shows that the cold-wall boundary condition results in a much thinner boundary layer than was computed for the hot-wall conditions. This

thinner, cold-wall boundary layer is also less susceptible to separation than were the hot-wall results. Also note that the thinner cold-wall boundary condition provides expansion that is more nearly like the one-dimensional case than were the hot-wall results.

The effects of changing Reynolds number in the conical nozzle can be seen by comparing the $p_o = 35$ atm results in Fig. 12 with the $p_o = 3.5$ atm results in Fig. 6. Here, only the extrapolated results are shown, but the very thin boundary layer and the increased expansion at the higher Reynolds number is readily noted.

As a final comparison, results for the contoured nozzle are shown in Fig. 13 for the low Reynolds number case (3.5 atm) at both 3000 K and 300 K. The effects of wall temperature on this contoured nozzle are shown directly in Fig. 13. The effects of Reynolds number can be seen by comparing the results in Fig. 13 with those in Fig. 8. Again, lower Reynolds numbers cause a dramatic increase in the boundary-layer thickness. Also, the Reynolds number change is sufficient so that the boundary is no longer truly turbulent, and its character reverts toward a laminar behavior, although the turbulence model is still included.

Verification of Global Conservation

Because our interests are in predicting thrust, accurate maintenance of global conservation is of paramount importance for our nozzle flowfield calculations. Accordingly, we have maintained an active check of global mass conservation throughout our studies. To demonstrate the necessity of using the fully conservative equations in flowfield without discontinuities, we have made a few computations with the so-called quasiconservative form of the equations for comparison. The quasiconservative formulation is identical to Eq. (1), except that the metric terms are left outside the derivatives:

$$\frac{\partial \boldsymbol{Q}}{\partial t} + \xi_x \frac{\partial \boldsymbol{E}}{\partial \xi} + \eta_x \frac{\partial \boldsymbol{E}}{\partial \eta} + \xi_y \frac{\partial \boldsymbol{F}}{\partial \xi} + \eta_y \frac{\partial \boldsymbol{F}}{\partial \eta} = \boldsymbol{H} \tag{8}$$

The fully conservative formulation maintained mass conservation to within 1% throughout the length of the nozzle, whereas the quasiconservative formulation allowed a global mass error that approached 30%. The reason for this is that although the quasiconservative form of the equations conserves mass to within a very small fraction between any two axial locations, the error at each location is correlated to the errors at locations around it. Thus, successive errors tend to add rather than cancel out. In all cases computed to date with the conservative formulation, including calculations for area ratios as large as 700 : 1, the maximum mass error has been maintained below 1%, with the exception of a case of a nozzle with a large separated region in which an error of 2.5% was observed. The reasons for this are still being investigated, but the results clearly show that the conservative formulation is the only one that is acceptable, even when the entire flowfield is continuous.

Conclusions

A hybrid discretization composed of central differencing in the cross-stream direction and second-order upwinding in the streamwise direction has been used to compute viscous supersonic flows in nozzles. Four different solution procedures, including three approximate factorizations and one direct method, have been used to solve the thin-layer Navier-Stokes equations by a time-marching method. Of the approximate techniques, the DDADI scheme of Lombard et al.[14] is shown to require the least number of iterations, but in terms of CPU time the PNS-ADI scheme developed here is equally fast. The direct method seems particularly suited to the high Reynolds number viscous flow problem because of the natural matrix partitioning that can be used, but the rapid convergence of the DDADI and PNS-ADI schemes allowed them to outperform the direct method. The direct method is, however, noted as being more robust than any approximate scheme.

Care was taken in the results to use appropriate downstream boundary conditions for the subsonic portions of the outflow. These downstream boundary conditions were shown to be capable of allowing the supersonic solutions to respond to nozzle back pressure conditions as they are observed to do in experimental situations. Calculations with recirculation and re-entry flow at the exit plane caused no difficulty, and results showed the exit pressure could be used to modify the nozzle boundary-layer characteristics near the exit plane. The extrapolation conditions that are normally used were shown to produce reasonable exit profiles that are almost equal to specified back pressure conditions (at one specific pressure). The extrapolated boundary conditions, however, resulted in a weak pressure gradient across the boundary layer at the exit plane, which was easily removed by specifying a proper downstream boundary condition. A series of results showing the effect of variations in back pressure, wall temperature, and nozzle Reynolds number are given for both a conical nozzle and a high expansion ratio contoured nozzle. Results of global mass conservation are also shown, which indicate that global mass conservation errors can be kept below 1% when a fully conservative scheme is used, but quasiconservative schemes can show global errors of more than 30%, even in flowfields without shocks.

Finally, we note that the extension of these algorithms to three-dimensional flows will require some sort of approximate factorization in the cross plane, and this approximation will reduce optimum CFL's and change convergence rates. We expect that the PNS-ADI or the DDADI schemes will still outperform traditional ADI methods, but in three dimensions artificial viscosity will probably be required in the cross plane if central differencing is used. In lieu of artificial viscosity, upwind can be used in the cross plane also.

Acknowledgment

This work was sponsored by the Rocket Propulsion Laboratory, Edwards Air Force Base, CA.

References

[1]Vigneron, Y. C., Rakich, J. V., and Tannehill, J. C., "Calculation of Supersonic Viscous Flow Over Delta Wings with Sharp Subsonic Leading Edges," AIAA Paper 78-1137, July 1978.

[2]Lawrence, S. L. and Tannehill, J. C., "An Upwind Algorithm for the Parabolized Navier-Stokes Equations," AIAA Paper 86-1117, May 1986.

[3]Power, G. D. and Anderson, O. L., "Assessment of a Parabolic Analysis for Axisymmetric Internal Flows in Rocket and Turbomachinery Ducts," AIAA Paper 86-1598, June 1986.

[4]Gielda, T. and McRae, D., "An Accurate, Stable, Explicit, Parabolized Navier-Stokes Solver for High Speed Flows," AIAA Paper 86-1116, May 1986.

[5]Baldwin, B. S. and Lomax, H., "Thin Layer Approximation and Algebraic Model for Separated Turbulent Flows," AIAA Paper 78-0257, Jan. 1978.

[6]Vuong, S. T. and Coakley, T. J., "Modeling of Turbulence for Hypersonic Flows With and Without Separation," AIAA Paper 87-0286, Jan. 1987.

[7]Shirazi, S. A. and Truman, C. R., "Comparison of Algebraic Turbulence Models for PNS Predictions of Supersonic Flow Past a Sphere-Cone," AIAA Paper 87-0544, Jan. 1987.

[8]Rubin, S. G., "A Review of Marching Procedures for Parabolized Navier-Stokes Equations," *Proceedings of Symposium on Numerical and Physical Aspects of Aerodynamic Flows*, edited by T. Cebeci, Springer-Verlag, New York, 1982, pp. 171–186.

[9]Lin, A. and Rubin, S. G., "Three-Dimensional Supersonic Vis-

cous Flow Over a Cone at Incidence," *AIAA Journal*, Vol. 20, Nov. 1982, pp. 1500–1507.

[10]Rakich, J. V., "Iterative PNS Method for Attached Flows with Upstream Influence," AIAA Paper 83-1955, June 1983.

[11]Steger, J. L. and Warming, R. F., "Flux Vector Splitting of the Inviscid Gasdynamic Equations with Application to Finite Differences Methods," NASA TM-78605, July 1979.

[12]Warming, R. F. and Beam, R. M., "On the Computation and Application Implicit Factored Schemes for Conservation Laws," *SIAM-AMS Proceedings*, Vol. 11, Jan. 1978, pp. 85–129.

[13]Briley, W. R. and McDonald, H., "On the Structure and Use of Linearized Block Implicit Schemes," *Journal of Computational Physics*, Vol. 34, Feb. 1980, pp. 54–73.

[14]Lombard, C. K., Bardina, J., Venkatapathy, E., and Oliger, J., "Multi-Dimensional Formulation of CSCM—An Upwind Flux Difference Eigenvector Split Method for the Compressible Navier-Stokes Equations," AIAA Paper 83-1895, July 1983.

[15]Lombard, C. K., Venkatapathy, E., and Bardina, J., "Universal Single-Level Implicit Algorithm for Gasdynamics," AIAA Paper 84-1533, June 1984.

[16]Chakravarthy, S. R., "Relaxation Methods for Unfactored Implicit Upwind Schemes," AIAA Paper 84-0165, Jan. 1984.

[17]MacCormack, R. W., "Current Status of Numerical Solutions of the Navier-Stokes Equations," AIAA Paper 85-0032, Jan. 1985.

[18]Merkle, C. L. and Chang, C.-L., "The Relation Between Flux Vector Splitting and Parabolized Schemes," *Journal of Computational Physics*, (to be published).

[19]Choi, Y.-H., Merkle, C. L., and Lawson, C. W., "Numerical Modeling of Low Speed Flows with Heat and Mass Diffusion," AIAA Paper 88-0745, Jan. 1988.

[20]Hoffman, R. J., Hetrick, M. A., Jr., Nickerson, G. R., and Jarossy, F. J., *Plume Contamination Effects Prediction: CONTAM III-Computer Program*, Vols. 1–3, Air Force Rocket Propulsion Lab., Edwards AFB, CA, AFRPL-TR-82-033, Dec. 1982.